A Janus Logic Gate with Sensing Function

Junyang Sui, Siyuan Liao, Ruiyang Dong, and Hai-Feng Zhang

A layered metastructure (LM) formed by a quasi-periodic arrangement of graphene and isotropic dielectric mediums, which can realize the functions of the tunable logic gate and refractive index (RI) sensing based on spin Hall effect (SHE), is theoretically studied. The asymmetric arrangement of the mediums and the increased angle of the incident electromagnetic waves (EWs) equip the LM with Janus feature. Through the modulation of the graphene chemical potential, the sharp absorption peak (AP) in the terahertz (THz) range can be obtained, and then the AP can be used to implement NOT logic and OR logic respectively corresponding to the forward and backward scales. By locating the incident angle of light corresponding to the SHE displacement peak, the linear measurement relationship between RI and SHE angle can be realized, and the widest RI measurement range is 1–1.4 with the angles changing from 21.88° to 61.84°. Additionally, a good linear range can be achieved, owning the optimum sensitivity (S) up to 153.5° RIU^{-1}. The RI sensing still strictly follows the logic functions of the forward NOT and backward OR via adjusting the chemical potential of graphene and discriminating the peak value of SHE displacement.

1. Introduction

Janus, the Roman god of creation, has two faces, one facing the past and the other facing future. Layered metastructure (LM) is a quasi-periodic structure formed by artificially filled media, which has physical properties and functions that are not found in natural structures, such as black hole,[1] absorption,[2] and stealth.[3] When done by means such as asymmetric arrangement,[4] and anisotropic media introduction,[5] different electromagnetic characteristics and performance are presented under the electromagnetic waves (EWs) propagating forward and backward in LM. Inspired by Roman mythology, scientists call this phenomenon the Janus property of LM.[6]

With the deepening of LM research, graphene has become a hot research topic because of the electronic properties and optical

J. Sui, S. Liao, H.-F. Zhang
College of Electronic and Optical Engineering & College of Flexible Electronics (Future Technology)
Nanjing University of Posts and Telecommunications (NJUPT)
Nanjing 210023, P. R. China
E-mail: hanlor@njup.edu.cn; hanlor@163.com
R. Dong
Bell Honors School
Nanjing University of Posts and Telecommunications (NJUPT)
Nanjing 210023, P. R. China

The ORCID identification number(s) for the author(s) of this article can be found under https://doi.org/10.1002/andp.202200661

such as ballistic transmission and saturation absorption.[7] Studies in recent years have shown that photoconduction can be influenced by changing the chemical potential μ_C or Fermi energy E_f, so the electromagnetic properties of graphene can be modulated by the applied voltage.[8] In comparison with other tunable materials,[9] graphene has the characteristics of simple structure, high efficiency, and easy integration, which brings a more excellent solution for optical dynamic modulator components. Moreover, it has realized the control of parameters such as absorption,[10] scattering field polarization,[11] and phase.[12] The spin Hall effect (SHE) refers to the phenomenon that in the process of total reflection, due to the conservation of spin angular momentum and orbital angular momentum, the left-handed circular polarization component and right-handed circular polarization component of the line-polarized light are divided into two beams of light with different horizontal directions according to the direction of rotation.[13] The lateral splits caused by SHE are so small that they are usually at sub-wavelength scales and are difficult to observe in experiments. Hosten et al. proposed a method of weak measurement,[14] and related studies prove that the use of Brewster angle,[15] surface plasmon resonance effect,[16] and optical tunneling effect can significantly enhance SHE,[17] making it possible to observe the split size of SHE.

With the continuous advancement of research, LM that can be used for logic gates or using SHE for physical quantity sensing have been widely studied. Anusooya et al. based on photonic crystals ring resonators presented the design of all-optical NAND and NOR gates,[18] and the function of the all-optical gates depended on the principle of the ring resonator and the intensity of incident light. Srivastava et al. studied a surface plasmon resonance sensor which can use photon SHE to detect the refractive index (RI) of biomolecules.[19] It was found that if the RI of the sensing layer changes very little, the lateral spin-dependent displacement can be changed, and the detection S can reach 1.5×10^5 µm RIU^{-1}. Dong et al. effectively modulated the Fermi energy level of graphene and significantly enhanced SHE by adding a light pump,[20] and under the condition of 0.4 w optical pumping power, using the displacement and angle of SHE, an accurate measurement of the RI in the range of 1.65998–1.66179 could be used to distinguish between normal cells and cancer cells, which provided a new idea for enhancing SHE. Unfortunately, these

Table 1. The Janus performance of the LM.

	Logic gate	RI sensing range	RI sensing S
Forward	NOT gate	1–1.4	97.72 ° RIU^{-1}
Backward	OR gate	1.33–1.58	135.5 ° RIU^{-1}
		1.33–1.39	153.5° RIU^{-1}
		1.33–1.6	142.8° RIU^{-1}

studies focused only on the continuous improvement of the performance of the device and did not achieve multi-functionality. Youngblood et al. produced a graphene device that could efficiently provide both light modulation and light detection functions. This provides new ideas for the study of LM.[21]

In this paper, a multi-function one-dimensional (1-D) LM based on chemical potential μ_C of graphene layer (GL) tuning is proposed. Due to the asymmetrical arrangement of the mediums and the increased incidence angle of EWs, the LM owns good Janus feature. **Table 1** indicates the Janus property of the LM in terms of multi-function. The sharp absorption peak (AP) is produced via the intrinsic absorption of GL. By modulating the GL chemical potential and locating the AP frequency point, the OR logic function can be implemented at the same frequency point when the EWs propagate forward. Similarly, NOT logic gates can be implemented on the backward scale. By locking the incident angle corresponding to the SHE displacement peak, RI sensing can be achieved which gains better sensitivity (S). At the different frequencies of incident EWs on the forward and backward scales, RI and SHE angles indicate a good measurement relationship. Furthermore, by regulating the GL chemical potential and discriminating the peak value of SHE displacement, the RI sensing can be achieved strictly following the NOT logic and OR logic respectively corresponding to the forward and backward scales. It is a highlight of this article. This multi-scale, versatile, and multi-logic LM is the supplement of traditional single-function LM and has a certain research prospect.

2. Design and Discussion

2.1. The Theoretical Model

The structure can be feasibly manufactured in the experiment according to the etching methods provided in refs. [22–24], which is widely used in the fabrication of the layered metastructure. Since this paper focuses on theoretical research, it will not be discussed here. **Figure 1**a displays the configuration of a 1-D LM. The red and blue arrows separately indicate that EWs incident from forward and backward directions, forming an angle θ with the xoz plane. Figure 1a also shows the settings for a Gaussian beam to shoot into a certain angle spectrum on the surface of the first layer, using purple and green beams to severally represent the left-handed and right-handed polarization components. To adapt the unit to the general situation, the temperature T is set to 270 K. The thickness of ordinary dielectric mediums A, B, C, and D is separately set to $d_A = 6.875$ μm, $d_B = 13.75$ μm, $d_C = 5$ μm, and $d_D = 5.5$ μm. The RI of ordinary dielectrics are $n_A = 2$, and $n_D = 5$. The dielectric B is air and the RI is $n_B = 1$. Material C selects barium strontium titanate doped by 10 wt% MgO,

which owns high permittivity ($\varepsilon_C = 272$), so the RI of medium C is $n_C = 16.49$.[25,26] It should be emphasized that Leiwin et al. derived effective permittivity and permeability expressions for composites based on Mie resonance theory, and the desired RI can be obtained in a wide range.[27] This technology has been applied in practice,[28] so the permittivity set in this paper is reasonable and can be obtained in reality. The mediums that make up the LM contain two different GLs which are GL$_1$ and GL$_2$ with thicknesses of $d_1 = 0.34$ nm and $d_2 = 0.34$ nm, and their chemical potentials are μ_{C1} and μ_{C2}, respectively. μ_C indicates the externally controllable chemical potential of the GL by modulating the external voltage. The feeding mode of GL is indicated in Figure 1b. The entire structure is placed on a silicon dioxide substrate, the gold electrodes at the top and bottom of the structure are in direct contact with the GLs, and a forward gate bias is applied to the gold electrode at the top. A negative voltage is connected to the gold electrode at the bottom. Therefore, applying direct-current bias voltage can effectively regulate the chemical potential of GL,[29] which gives graphene a huge advantage when designing tunable LMs. The conductivity σ of GL consists of intraband σ_{intra} and interband σ_{inter}.[30]

$$\sigma = \frac{ie^2 k_B T}{\pi \hbar^2 (\omega + i/\tau)} \left(\frac{\mu_C}{k_B T} + 2\ln(e^{-\frac{\mu_C}{k_B T}} + 1) \right)$$
$$+ \frac{ie^2}{4\pi\hbar} \ln \left| \frac{2\mu_C - \hbar(\omega + i/\tau)}{2\mu_C + \hbar(\omega + i/\tau)} \right| \tag{1}$$

where ω, k_B, $\hbar$, e, T, μ_C, τ respectively represent angular frequency, Boltzmann's constant, Planck's constant, electron charge, temperature, chemical potential, and carrier relaxation time. Due to the dependence of graphene conductivity on chemical potential, we can change the conductivity of GL by regulating the chemical potential to achieve the modulation function. Assuming that the electronic energy band of a GL is not affected by adjacent elements, the effective dielectric constant ε_G of GL can be written as:[30]

$$\varepsilon_G = 1 + \frac{i\sigma}{\omega \varepsilon_0 d_j} \tag{2}$$

where ε_0 and d_j ($j = 1$ or 2) represent the vacuum dielectric constant and the thickness of the GL, respectively. So, the RI of GL is written as $n_G = (\varepsilon_G)^{1/2}$. For the ordinary media layers and GLs, their transfer matrices can be expressed as:[31]

$$\mathbf{M}_i = \begin{pmatrix} \cos(k_{iz}d_i) & -\frac{i}{\eta_i}\sin(k_{iz}d_i) \\ -i\eta_i \sin(k_{iz}d_i) & \cos(k_{iz}d_i) \end{pmatrix} \tag{3}$$

among them, i can be represented by A, B, C, D, 1, and 2, symbolizing the transmission matrices of different ordinary mediums, GL$_1$ and GL$_2$. $k_{jz} = \omega/cn_i \sin\theta_i$ is the component of the wave vector on the z-axis, and the speed of light in a vacuum is symbolized by c. The definition of s-wave and p-wave can be referred to refs. [32–34] η_i is the light conductivity, for s-wave, $\eta_i = (\varepsilon_0/\mu_0)^{1/2} n_i \cos\theta_i$. For p-wave, then $\eta_i = (\varepsilon_0/\mu_0)^{1/2} n_i / \cos\theta_i$. ε_0 and μ_0 are vacuum dielectric constants and permeability, respectively. The transmis-

**ADVANCED
SCIENCE NEWS**

www.advancedsciencenews.com
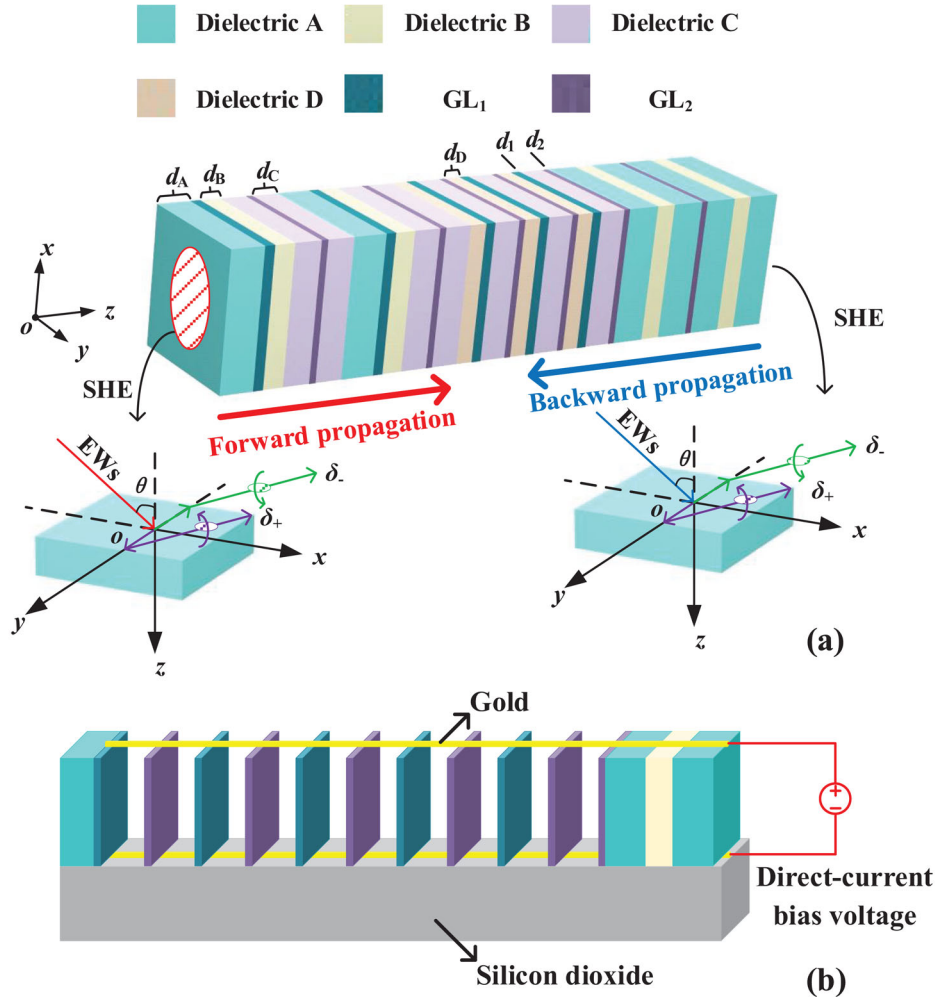
annalen
der **physik**

www.ann-phys.org

Figure 1. a) The diagram of the proposed LM which is composed of GLs and ordinary dielectric mediums A, B, C, and D filled with different colors. Through an asymmetric arrangement of the dielectric layers, the overall structure $(AGL_1BCGL_2C)^2(DGL1CGL_2)^2DGL_1C(GL_1ABA)^2$ is finally formed. b) The schematic view of the feeding belonging to GLs.

sion matrix of $(AGL_1BCGL_2C)^2(DGL_1CGL_2)^2DGL_1C(GL_1ABA)^2$ is:[31]

$$\mathbf{M} = \sum_{i}^{26} M_i = \begin{pmatrix} m_{11} & m_{12} \\ m_{21} & m_{22} \end{pmatrix} \tag{4}$$

The reflection and transmission coefficients are symbolized by r and t can be expressed as:[31]

$$r = \frac{(M_{11} + M_{12}\eta_0)\eta_0 - (M_{21} + M_{22}\eta_0)}{(M_{11} + M_{12}\eta_0)\eta_0 + (M_{21} + M_{22}\eta_0)} \tag{5}$$

$$t = \frac{2\eta_0}{(M_{11} + M_{12}\eta_0)\eta_0 + (M_{21} + M_{22}\eta_0)} \tag{6}$$

The $R = |r|^2$ and $T = |t|^2$ separately represent reflectance (R) and transmittance (T). The absorptance (A) is written through:[31]

$$A = 1 - R - T \tag{7}$$

Gaussian beams with a certain angle spectrum can be expressed as:[35]

$$\tilde{E}i\pm = (eix + ioei y)\frac{\omega_0}{\sqrt{2\pi}}\exp\left[-\frac{\omega_0^2(k_{ix}^2 + k_{iy}^2)}{4}\right] \tag{8}$$

where ω_0 represents the beam waist and o is the polarization operator. Left-handed and right-handed circular polarized beams are respectively represented by $o = 1$ and $o = -1$. The horizontal and vertical polarization states are separately symbolized by H and V. A matrix of coefficients between an incident and reflected electric fields can be expressed as:[35]

$$\begin{bmatrix} \tilde{E}_r^H \\ \tilde{E}_r^V \end{bmatrix} = \begin{bmatrix} r^p & \frac{kr\gamma\cot\theta_i(r^p+r^s)}{k_0} \\ -\frac{kr\gamma\cot\theta_i(r^p+r^s)}{k_0} & r^s \end{bmatrix} \begin{bmatrix} \tilde{E}_i^H \\ \tilde{E}_i^V \end{bmatrix} \tag{9}$$

k_0 symbolizes the number of waves in free space. r^p and r^s represent the Fresnel reflection coefficients of the p-wave and s-wave,
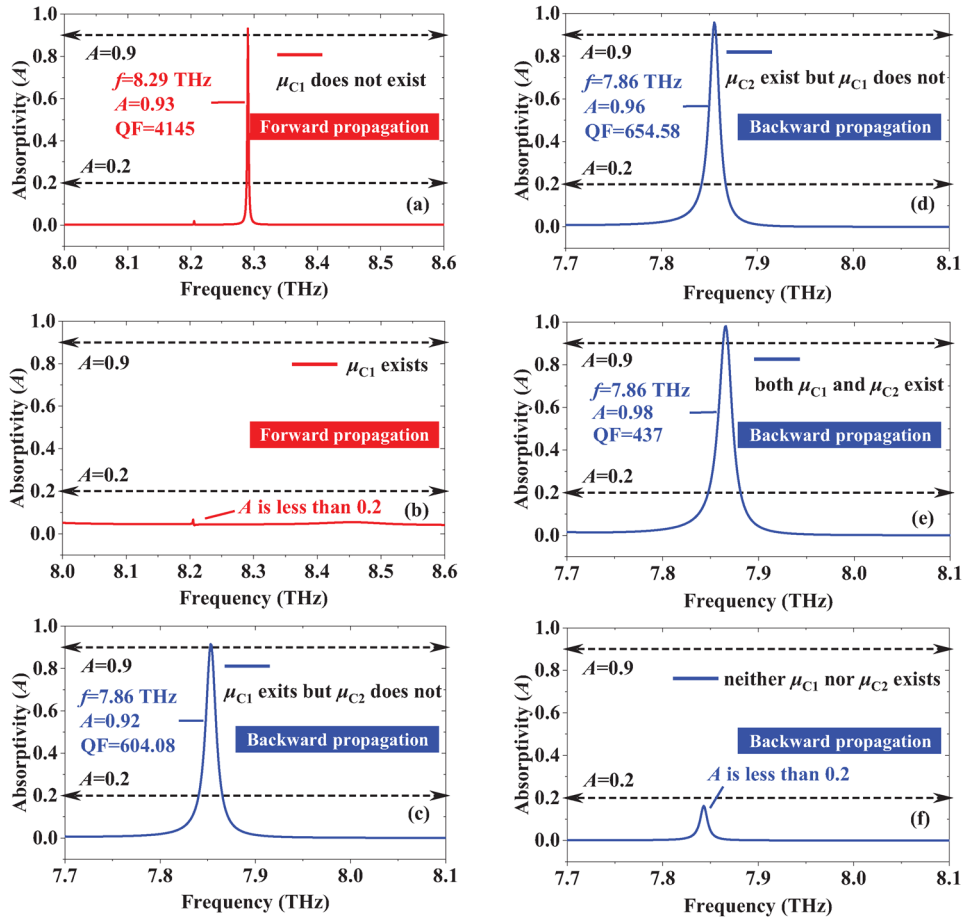
**ADVANCED
SCIENCE NEWS**

www.advancedsciencenews.com

annalen
der **physik**

www.ann-phys.org

Figure 2. Schematic diagrams of μ_C modulated logic gates and APs. The NOT logic on the forward scale: a) μ_{C1} does not exist, and b) μ_{C1} exists. The OR logic on the backward scale: c) "1 OR 0 = 1," d) "0 OR 1 = 1," e) "1 OR 1 = 1," and f) "0 OR 0 = 0."

respectively. According to Equations (8) and (9), we can obtain the expression of the spectrum of the reflection angle:[35]

$$\tilde{E}_r^H = \frac{r_p}{\sqrt{2}}[\exp\left(+ik_{ry}\delta_r^H\right)\tilde{E}_{r+} + \exp\left(-ik_{ry}\delta_r^H\right)\tilde{E}_{r-}]$$
$$\tilde{E}_r^V = \frac{ir_s}{\sqrt{2}}[-\exp\left(+ik_{ry}\delta_r^V\right)\tilde{E}_{r+} + \exp\left(-ik_{ry}\delta_r^V\right)\tilde{E}_{r-}]$$
(10)

Here, $\delta_r^H = (1+r^s/r^p)\cot\theta_i/k_0$ and $\delta_r^V = (1+r^p/r^s)\cot\theta_i/k_0$. $\tilde{E}_{r\pm}$ can be written in a similar style to Equation (8). φ^s and φ^p symbolize the phase of r^s and r^p. For the reflected light, the SHE lateral displacement of the left-handed and right-handed components can be expressed as:[35]

$$\delta_\pm^H = \mp\frac{\lambda}{2\pi}\left[1 + \frac{|r^s|}{|r^p|}\cos(\varphi^s - \varphi^p)\right]\cot\theta_i$$
$$\delta_\pm^V = \mp\frac{\lambda}{2\pi}[1 + \frac{|r^p|}{|r^s|}\cos(\varphi^p - \varphi^s)]\cot\theta_i$$
(11)

In this paper, we only discuss the case of left-handed circularly polarized components displacement δ_+^H.

2.2. Analysis and Discussion of Performances

When the chemical formulas μ_{C1} and μ_{C2} of GL_1 and GL_2 change, the corresponding absorptivity (A) patterns of the forward NOT logic gate and the backward OR logic gate on the THz band are indicated in **Figure 2**. The EWs are incident at an angle of 70°. Due to the modulation of the chemical potential of GL and the increased angle of incidence, the Janus feature of LM on the forward and backward scales is enhanced. The μ_C can adjust the RI of GL, thus affecting the modulation of the wave vector and phase of the incident light, and affecting the position of the resonant frequency of AP. By accurately calculating and parameter optimizing each layer, the function of different logic gates in the front and back direction can be realized. Two chemical potentials corresponding to different GLs are considered input logic levels. The μ_{C1} of GL_1 indicates the first input, and the μ_{C2} of GL_2 symbolizes the second input. "In_1" and "In_2" represent the present state of the μ_{C1} and μ_{C2}, respectively, and "Ou" is on the behalf of the state of the output quantity. When the μ_C is present ($\mu_C = 0.8$ eV), the input LL is "In = 1". The μ_C does not exist, that is, when $\mu_C = 0$ eV, the input LL is "In = 0." When AP is greater than 0.9, it means that the output LL "Ou" is "1," and if it is less than 0.2, that is, "Ou = 0." When EWs are incident from forward, under the condition of the μ_{C2} of GL_2 being set to 0 eV, that is, it does not exist, a NOT logic gate can be implemented by the μ_{C1} of GL_1 modulation. Figure 2a indicates that, when the μ_{C1} on the forward scale is absent, the sharp AP ($A > 0.9$) is generated, indicating "$In_1 = 0$," and "Ou = 1" for NOT logic. The frequency

**ADVANCED
SCIENCE NEWS**

www.advancedsciencenews.com

annalen
der **physik**

www.ann-phys.org

Table 2. Logical truth value table. (The present state of chemical potential μ_C is indicated in parentheses).

	In1	In2	Ou
NOT	0	0	1
	1 (μ_{C1} exists)	0	0
OR	1 (μ_{C1} exists)	0	1
	0	1 (μ_{C2} exists)	1
	1 (μ_{C1} exists)	1 (μ_{C2} exists)	1
	0	0	0
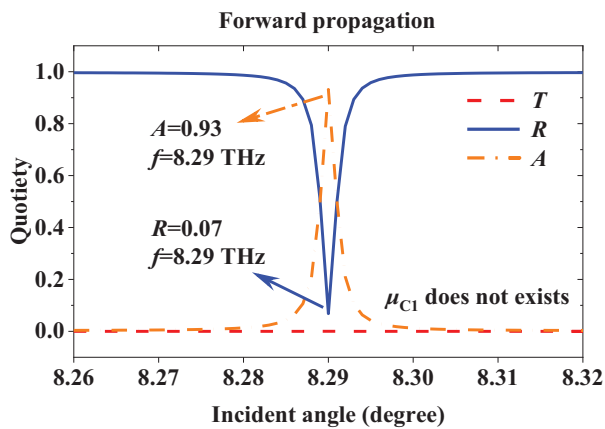
Figure 3. The T, R, and A when EWs propagate forward and μ_{C1} does not exist.

Figure 4. The A spectra belonging to different μ_{C1} when EWs propagate forward and μ_{C2} does not exist.

point of AP is 8.29 THz, and the A, quality factor (QF) belonging to it is 0.93, 4145. As shown in Figure 2b, when the μ_{C1} is present, no sharp AP is generated, and A is much smaller than 0.2, strictly following the NOT logic: "In$_1$ = 1," "Ou = 0." Figures 2c–e are the A patterns in the presence of either or both μ_{C1} and μ_{C2} for EWs backward propagating, respectively. It can be seen that sharp APs exist, and their frequency points f is the same, at 7.86 THz. The difference between the frequency points belonging to the forward and backward APs is 0.43 THz, which reflects Janus property. The A of these conditions are severally 0.92, 0.96, and 0.98, satisfying the output LL "1," which corresponds accurately to the OR logical operations "1 OR 0 = 1," "0 OR 1 = 1," and "1 OR 1 = 1." And the relevant QF values are 604.08, 654.58, and 437, probing that they are sharp and easy to observe. Figure 2f is a case where the μ_{C1} and μ_{C2} are absent, and it can be seen that A is less than 0.2, which conforms to the OR logic operation of "0 OR 0 = 0." It can be seen that the LM is modulated by the chemical potentials of GL$_1$ and GL$_2$, and the NOT and OR logic operation functions are strictly implemented on the forward and backward scales, separately, owning different QF values, and the truth value table can be seen in **Table 2**.

For how to measure the A, we separately calculate the T and R of the same case, which can be measured easily. Then the corresponding A can be gained by Equation (7). **Figure 3** displays the T, R, and A curves at $\mu_{C1} = 0$ eV when EWs are incident forward. In Figure 2a, the frequency point of 8.29 THz the AP located is selected, and the corresponding T is close to 0 and $R = 0.07$, so $A = 0.93$ can be obtained via Equation (7), which is consistent.
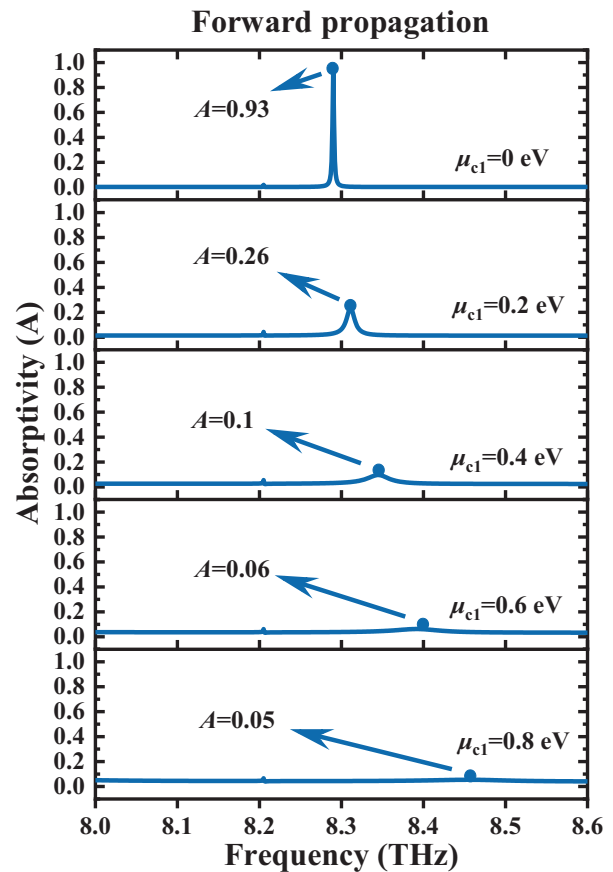
To illustrate the selection of $\mu_C = 0$ eV and $\mu_C = 0.8$ eV, which represent the presence or absence of the chemical potential of GL, **Figure 4** also takes the case of EWs incident from the font and μ_{C2} is set at 0 eV as an example and shows the A spectra of $\mu_{C1} = 0$ eV, $\mu_{C1} = 0.2$ eV, $\mu_{C1} = 0.4$ eV, $\mu_{C1} = 0.6$ eV, and $\mu_{C1} = 0.8$ eV, separately. It can be obviously seen that the value of AP decreases rapidly with the gradual increase of μ_{C1}. To highlight the difference between output LL "1" and "0" as much as possible, $\mu_{C1} = 0$ eV and $\mu_{C1} = 0.8$ eV corresponding to the maximum and minimum A are selected.

To explain the principle of sharp AP generation, we plotted the electric field energy distribution which owns an obvious phenomenon when EWs are incident backward at frequency $f = 7.86$ THz, the chemical potential μ_{C2} is present, and μ_{C1} does not. In **Figure 5**, the electric field intensity can be seen concentrating in the GL$_2$ and increasing rapidly, resulting in sharp AP. This is because GL is characterized by intrinsic absorption, causing GL absorbs more energy.

The chemical potential of graphene is an important parameter for modulating the photoconductivity of GL, and the change of photoconductivity will further cause the change of the Fresnel reflection coefficients and the δ^H_+ of the reflected light. To explain the generation of peak δ^H_+ and the regulation of δ^H_+ by μ_C, **Figure 6** indicates the curves of Fresnel reflection coefficients
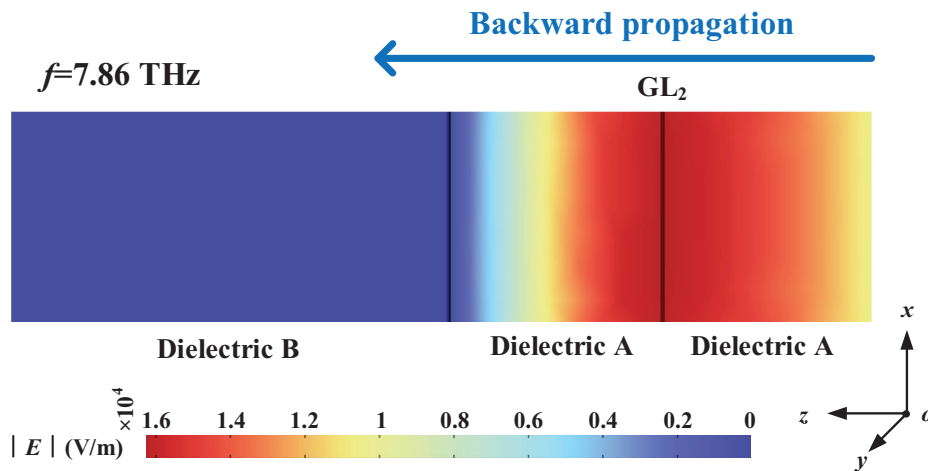
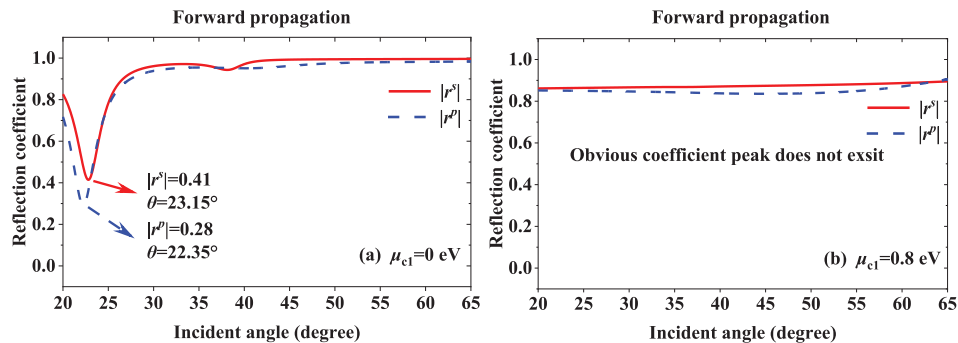**Figure 5.** Electric field distribution diagram at $f = 7.86$ THz when EWs propagate backward.

Figure 6. Under the condition of $\mu_{C2} = 0$ eV, reflection coefficient curves of $|r^s|$ and $|r^p|$ at different μ_{C1} when EWs propagate forward. a) $\mu_{C1} = 0$ eV. b) $\mu_{C1} = 0.8$ eV.

$|r^s|$, $|r^p|$ for different μ_{C1} when EWs propagate forward and μ_{C2} is set at 0 eV. According to Figure 6a, when $\mu_{C1} = 0$ eV, $|r^s|$ and $|r^p|$ have coefficient peaks at a certain incident angle. The values of $|r^s|$ and $|r^p|$ at the angle of incidence near the peak decreased rapidly. When $\mu_{C1} = 0.8$ eV, there is no obvious coefficient peak in Figure 6b. Indicated by the expression of SHE displacement Equation (11), the value of spin-correlated splitting mainly hinges on the $|r^s|/|r^p|$ part, so the value of $|r^s|/|r^p|$ can reach a large value near the peak of a rapid decline of $|r^p|$, resulting in the peak of δ^H_+. As shown in Figure 6a, when $\mu_{C1} = 0$ eV, there is a peak of δ^H_+. However, when $\mu_{C1} = 0.8$ eV, there is no obvious peak. Therefore, the δ^H_+ peak is regulated by μ_C.

Figure 7 displays the relationship between the displacement δ^H_+ and the incident angle θ of the SHE left-handed circularly polarized beam under different conditions of the present states of μ_{C1} and μ_{C2} on the forward and backward scales. Setting the displacement δ^H_+ positive along the y-axis and the SHE displacement phenomenon is obvious and reaches a peak. In Figure 7a, under the condition of $n_B = 1$, the peak of δ^H_+ is 1.58×10^{-5} m in the absence of μ_{C1}. The corresponding angle is $21.87°$. To measure the RI of dielectric B in different ranges forward and backward, therefore, n_B is set at 1.33 when EWs propagate backward at a frequency of 5.2 THz. Similarly, as shown in

Figure 7b, only μ_{C1} exists, only μ_{C2} exists, both exist and neither exist, their peaks are 3.85×10^{-5} m, 7.43×10^{-6} m, 7.19×10^{-6} m, and -1.53×10^{-5} m. The relative angles are $32.74°$, $61°$, $27.71°$, and $56.87°$. This can be explained by the fact that the peaks of the Fresnel reflection coefficients $|r^s|$ and $|r^p|$ curves are at different angles, and the value varies greatly at the same angle, so the SHE displacement is large. Same as above, in the presence or absence of the μ_C, the corresponding inputs LL is "1" or "0," respectively. The difference is that the output LL "Ou = 1" symbolizes the peak of δ^H_+ is greater than 3×10^{-6} m, and if the value of δ^H_+ is less than 3×10^{-6} m, that is, it moves along the $-y$-axis, the output LL is "Ou = 0." Since 3×10^{-6} m is small enough compared to other peaks with outputs of "Ou = 1," it is easy to distinguish them by weak measurements.[14] After the calculation and optimization of the incident EWs frequency and LM parameters, when EWs propagate forward, making the EWs propagate forward at 5.3 THz, μ_{C2} does not exist ($\mu_{C2} = 0$ eV), μ_{C1} changing between states of existence ($\mu_{C1} = 0.8$ eV) and non-existence ($\mu_{C1} = 0$ eV). Similarly, when EWs propagate backward at 5.2 THz, μ_{C1} and μ_{C2} vary between present and absent states. By locating the angle of SHE displacement δ^H_+ peak, the sensing of n_B can be realized, owning a good linear fitting relationship (LFR). Furthermore, under the condition of achieving RI sensing, the forward NOT and
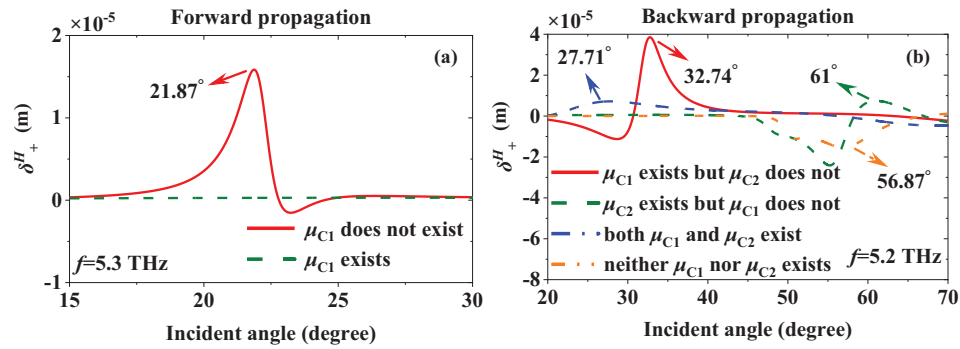
Figure 7. The SHE displacement δ^H_+ under different presence states of μ_{C1} and μ_{C2} on the forward and backward scales.
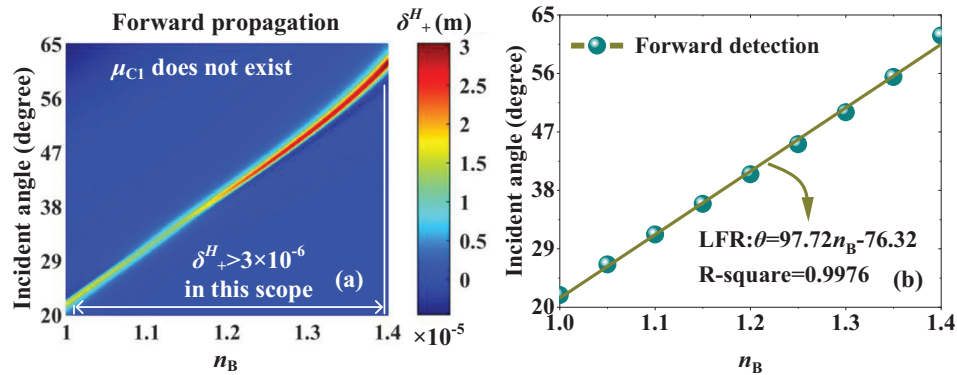

Figure 8. EWs propagate forward when μ_{C1} does not exist. a) The top view of δ^H_+ which uses for RI sensing, and b) the LFR between n_B and incident angle.

backward OR logic operations can be strictly followed via modulating GL chemical potential and judging the peak value of δ^H_+, which truth value table is indicated in Table 2. This is the highlight of this article.

Similar to the principle of modulation δ^H_+ by μ_C, the wave vector and phase of incident EWs will be affected by changing the RI of dielectric B, thus influencing the values of Fresnel reflection coefficients $|r^s|$ and $|r^p|$. Therefore, the change of n_B can also realize the modulation of δ^H_+. **Figures 8** and **9** respectively indicate the LFR between the angle of the δ^H_+ peak and n_B corresponding to the absence and presence of the μ_{C1} when μ_{C2} is fixed at 0 eV and EWs propagate forward at $f = 5.3$ THz. Figure 8a displays the x–y plane of the SHE displacement δ^H_+ peak surface map, intuitively illustrating the congruent relationship between RI and incident angle θ when $\mu_{C1} = 0$ eV ("In$_1 = 0$"). It can be seen that when the n_B increases from 1–1.4, the SHE displacement peaks grow rapidly from 21.88° to 61.84° which is quite significant. In addition, there is a LFR of SHE angle and n_B at the RI range of 1–1.4, which is worthy of attention for the sensor performance. And the peak value of δ^H_+ is above 3×10^{-6} m in this scope, which satisfies the NOT logic that the input LL is "In$_1 = 0$" and the output LL is "Ou $= 1$." To better analyze the RI detection performance of the LM, equidistant points are selected on the horizontal axis, and the LFR is obtained by linear fitting method. In this paper, R-square is used as the criterion of the linear fitting. As an important parameter for evaluating sensors, excellent sensors have
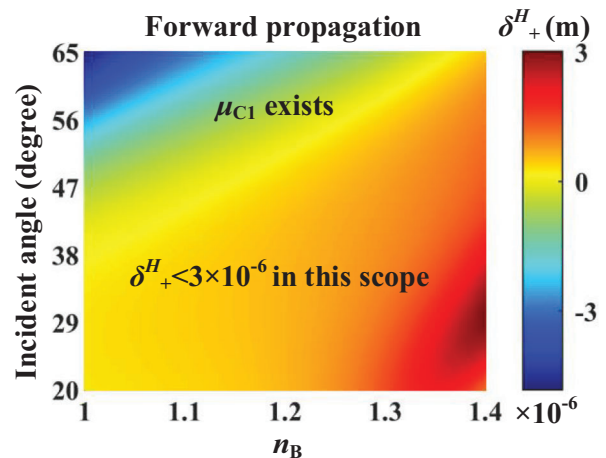

Figure 9. The top view of δ^H_+ varies with n_B under the presence of μ_{C1} when EWs propagate forward.

higher S. S corresponding definition can be expressed as follows, where $\Delta\theta$ and Δn_B refer to angle and RI changes.[36]
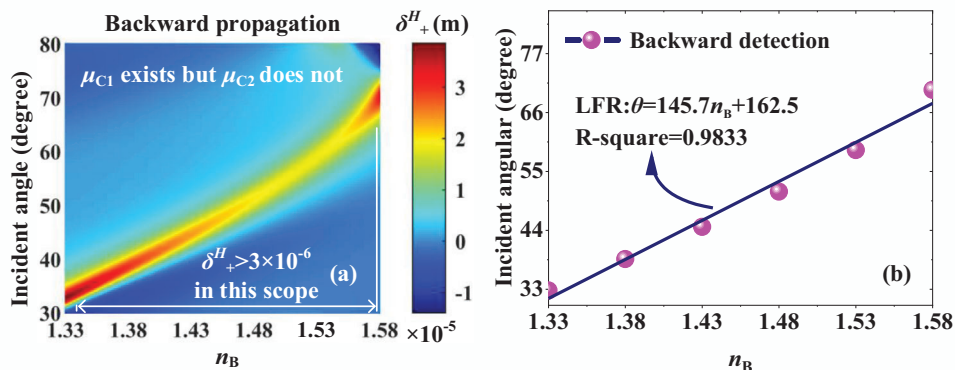
$$S = \frac{\Delta\theta}{\Delta nB} \tag{12}$$

Figure 10. EWs propagate backward when both μ_{C1} exists and μ_{C2} does not. a) The top view of δ^H_+ which uses for RI sensing, and b) the LFR between n_B and incident angle.
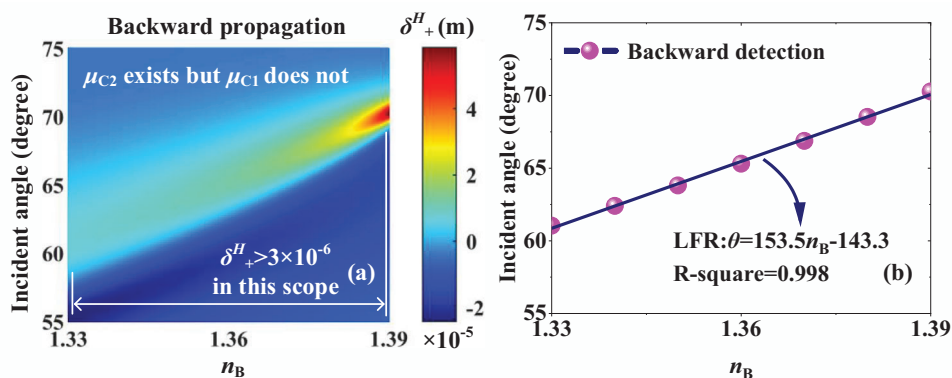

Figure 11. EWs propagate backward when μ_{C2} exists and μ_{C1} does not. a) The top view of δ^H_+ which uses for RI sensing, and b) the LFR between n_B and incident angle.

The fitting results between RI and SHE angles are indicated in Figure 8b. Its linear equation is $\theta = 97.72n_B-76.32$, and $97.72°$ RIU^{-1} is the S. The linearity of LFR can be reflected by the R-square. A higher value of R-square indicates a higher degree of fit and higher reliability of the LFR. Since R-square = 0.9976, the surface exhibits good linearity. Figure 9 shows the relationship between SHE angle and RI when $\mu_{C1} = 0.8$ eV ("In$_1$ = 1"). It can be seen that the value of δ^H_+ in the range of $n_B = 1–1.4$ is less than 3×10^{-6} m, indicating the output LL "Ou = 0," which is consistent with the logic operation of NOT.

For sensors, a single detection method often leads to poor accuracy of physical quantities, which can be improved if multiple detection methods are owning different S. We try to obtain RI sensing with different S by changing the existing states of μ_{C1} and μ_{C2}. When EWs propagate form backward at a frequency of 5.2 THz, the LFR of SHE angle and RI is presented in the $x-y$ plane in the presence of only one of or both the chemical potential μ_{C1} and μ_{C2}, as indicated in **Figures 10a**, **11a**, and **12a**. The peak of δ^H_+ corresponding to these cases is greater than 3×10^{-6} m in the scopes, indicating the output of "Ou = 1". Figures 10b and 11b exhibit the LFR in the presence of only μ_{C1} or μ_{C2}. when $n_B = 1.33–1.58$, and $1.33–1.39$, their linear equations are $\theta = 145.7n_B-162.5$, $\theta = 153.5n_B-143.3$. S is 145.7 and $153.5°$ RIU^{-1}, respectively, achieving sensitive detection. The cor-

responding R-squares are severally 0.9833 and 0.998, showing reliable linearity. Figure 12b displays the LFR under the condition of $\mu_{C1} = 0.8$ eV and $\mu_{C2} = 0.8$ eV. In the range of $n_B = 1.33–1.6$, its equation is $\theta = 142.8n_B-162.9$, with a good S of $142.8°$ RIU^{-1}. R-square = 0.9967 indicates good linearity. **Figure 13** indicates that in the absence of μ_{C1} and μ_{C2}, no δ^H_+ is greater than 3×10^{-6} m in the range of 1.33–1.6 of RI variation. In summary, $n_B = 1.33–1.39$ is the common RI sensing range of these cases, owning different S which can realize precise detection. And because the RI detection area is very small, it is suitable to detect small changes in RI, such as photochemical and biochemical virus detection. Additionally, in this range, the OR logic operations of "1 OR 1 = 1," "1 OR 0 = 1," "0 OR 1 = 1," and "0 OR 0 = 0" can be precisely kept.

To sum up, this LM owns the multi-function with multi-logic and RI sensing, and the parameters belonging to it are great. **Table 3** indicates the comparison of relative parameters between reported logic gates or RI sensing and the work of this paper. As can be seen from the parameters in Table 3, the given LM can fully meet the detection of RI. In addition, due to the Janus feature, the sensing range and S on the forward and backward scales are greatly different, and the measurement range is greatly increased. In the same range, different precision RI sensing can be achieved by different S.
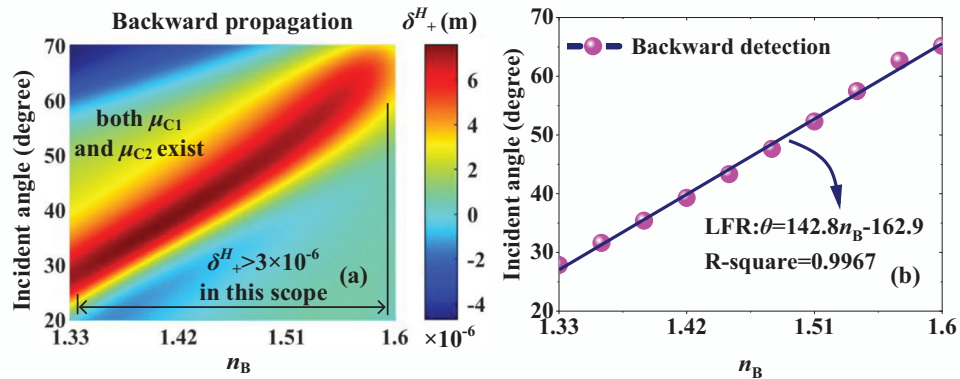
Figure 12. EWs propagate backward when both μ_{C1} and μ_{C2} exist. a) The top view of δ^H_+ which uses for RI sensing, and b) the LFR between n_B and incident angle.

Table 3. The performance of the published reports compared with such a LM.

Refs.	Janus	RI sensing	Logic gate	RI detection			Logic function
[37]	No	No	Yes	Range		None	OR
				S			
[38]	No	No	Yes	Range		None	XOR
				S			
[39]	No	No	Yes	Range		None	NAND
				S			NOR
[40]	No	No	Yes	Range		None	AND
				S			
[41]	No	Yes	No	Range		1.4–1.4028	None
				S		1.2×10^3 nm RIU^{-1}	
[42]	No	Yes	No	Range		1.3489–1.3715	None
				S		2.55 THz RIU^{-1}	
[43]	No	Yes	No	Range		1.3–1/44	None
				S		1100 nm RIU^{-1}	
[4]	Yes	Yes	No	Forward	Range	1.35–2.09	None
					S	132 MHz RIU^{-1}	
				Backward	Rang	1–1.57	
					S	40.7 MHz RIU^{-1}	
This work	Yes	Yes	Yes	Forward	Range	1–1.4	NOT
					S	97.72 ° RIU^{-1}	
				Backward	Range	1.33–1.6	OR
					S	142.8°RIU^{-1}	

3. Conclusions

In this paper, a LM based on GL is designed, which is endowed with Janus feature due to the asymmetry of the structure and the increased incidence angle of EWs. Sharp AP ($A > 0.9$) is obtained via the intrinsic absorption of graphene. And it can be modulated by the chemical potential μ_C, forming a multi-logic function of forwarding NOT and backward OR. By locating the angle of left-circularly polarized components displacement δ^H_+ peak, RI sensing owning different detection ranges and S corresponding to the cases of forwarding NOT logic and backward OR logic can be achieved, which the frequencies of incident EWs are severally 5.3 and 5.2 THz, indicating frequency division multiplexing function. And the ranges are 1–1.4 on the forward scale, 1.33–1.58, 1.33–1.39, and 1.33–1.6 on the backward scale, the relative S are respectively 97.72° RIU^{-1} on the forward scale, 135.5, 153.5, and 142.8° RIU^{-1} when EWs propagate backward. In addition, it can realize the accurate RI detection of multiple S in the range of 1.33–1.39. To sum up, the proposed Janus LM sensor has the characteristics of multi-logic and multi-function. Moreover, it is
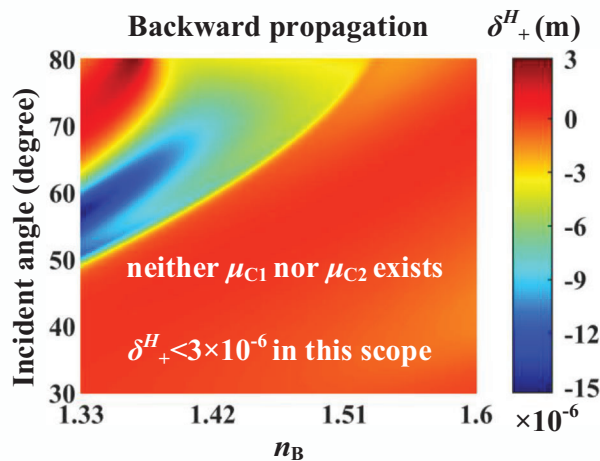
Figure 13. The top view of δ^H_+ varies with n_B under condition of neither μ_{C1} nor μ_{C2} exists when EWs propagate backward.

a supplement to the logic gates and sensors, which has certain theoretical research potential.

Conflict of Interest

The authors declare no conflict of interest.

Data Availability Statement

The data that support the findings of this study are available on request from the corresponding author. The data are not publicly available due to privacy or ethical restrictions.

[1] M. Yin, X. Yong Tian, H. Xue Han, *Appl. Phys. Lett.* **2012**, *100*, 124101.
[2] H. Xu, S. Bie, Y. Xu, *Composites, Part A* **2016**, *80*, 111.
[3] D. Schurig, J. J. Mock, B. J. Justice, *Science* **2006**, *314*, 977.
[4] Y. T. Xiang, B. F. Wan, H. F. Zhang, *IEEE Sens. J.* **2021**, *21*, 19984.
[5] S. H. Hu, X. Gao, *J. Am. Chem. Soc.* **2010**, *132*, 7234.
[6] A. Walther, A. H E Müller, *Soft Matter* **2008**, *4*, 663.
[7] A. G. Ardakani, *Eur. Phys. J. B.* **2015**, *88*, 166.
[8] Y. Zhang, T. T. Tang, C. Girit, *Nature* **2009**, *459*, 820.
[9] D. Wang, L. Zhang, Y. Gu, *Sci. Rep.* **2015**, *5*, 15020.
[10] Y. Fan, N. H. Shen, F. Zhang, *Adv. Opt. Mater.* **2019**, *7*, 1970009.
[11] A. V. Kildishev, A. Boltasseva, V. M. Shalaev, *Science* **2013**, *339*, 1232009.
[12] T. Yatooshi, A. Ishikawa, K. Tsuruta, *Appl. Phys. Lett.* **2015**, *107*, 053105.
[13] H. W. Dong, S. D. Zhao, Y. S. Wang, ArXiv Preprint ArXiv **2017**, *1730*, 03298.
[14] O. Hosten, P. Kwiat, *Science* **2008**, *319*, 787.
[15] H. Luo, X. Zhou, W. Shu, *Phys. Rev. A* **2011**, *84*, 1452.
[16] X. J. Tan, X. S Zhu, *Opt. Lett.* **2016**, *41*, 2478.
[17] X. Zhou, X. Ling, Z. Zhang, *Sci. Rep.* **2014**, *4*, 7388.
[18] V. Anusooya, S. Ponmalar, M. Manikandan, *Laser Phys.* **2012**, *32*, 016202.
[19] A. Srivastava, A. K. Sharma, Y. K Prajapati, *Chem. Phys. Lett.* **2021**, *774*, 138613.
[20] P. Dong, J. Cheng, H. Da, *New. J. Phys.* **2020**, *22*, 113007.
[21] N. Youngblood, Y. Anugrah, R. Ma, *Nano Lett.* **2014**, *14*, 2741.
[22] S. Guo, C. Hu, H. Zhang, *J. Opt.* **2020**, *22*, 105101.
[23] W. M. J. Green, J. Scheuer, G. DeRose, *Appl. Phys. Lett.* **2004**, *85*, 3669.
[24] J. Scheuer, A. Yariv, *J. Opt. Soc. Am. B.* **2003**, *20*, 2285.
[25] F. Zhang, S. Feng, K. Qiu, *Appl. Phys. Lett.* **2015**, *106*, 091907.
[26] F. Zhang, Z. Liu, K. Qiu, *Appl. Phys. Lett.* **2015**, *106*, 061906.
[27] L. Lewin, *J. Inst. Electr. Eng., Part 3* **1947**, *94*, 65.
[28] X. Liu, Z. Qian, C. Lan, *Appl. Phys. Lett.* **2013**, *103*, 4773.
[29] L. Qi, C. Liu, S. M. A. Shah, *Carbon* **2019**, *153*, 179.
[30] A. Andryieuski, A. V Lavrinenko, *Opt. Express* **2013**, *21*, 9144.
[31] L. Qi, Z. Yang, *Phys. Plasmas* **2010**, *17*, 042501.
[32] E. W Fenton, *Solid State Commun.* **1980**, *34*, 917.
[33] H. Y. Cheng, C. K. Chua, C. W Hwang, *Phys. Rev. D.* **2004**, *69*, 074025.
[34] S. Guo, S. Albin, *Opt. Express* **2003**, *11*, 167.
[35] C. Gao, B. Guo, *Phys. Plasmas* **2017**, *24*, 093520.
[36] Z. A. Zaky, A. M. Ahmed, A. S. Shalaby, *Sci. Rep.* **2020**, *10*, 9736.
[37] M. Pirzadi, A. Mir, D. Bodaghi, *IEEE Photonics Technol. Lett.* **2016**, *28*, 2387.
[38] K. Heydarian, A. Nosratpour, M. Razaghi, *J. Nonlinear Opt. Phys. Mater.* **2022**, *31*, 2250013.
[39] V. Anusooya, S. Ponmalar, M. S. K. Manikandan, *Laser Phys.* **2021**, *32*, 016202.
[40] K. Heydarian, A. Nosratpour, M. Razaghi, *Opt. Eng.* **2021**, *60*, 047104.
[41] Y. Chen, J. Dong, T. Liu, *Mod. Phys. Lett. B* **2016**, *30*, 1650030.
[42] B. F. Wan, Q. Y. Wang, H. M. Peng, *IEEE Sens. J.* **2021**, *21*, 21465.
[43] M. A. Rahman, T. Ahmed, M. I. Haque, *J. Sens. Technol.* **2022**, *12*, 1149.